



A comparative investigation of aging effects on thermal runaway behavior of lithium-ion batteries

Dongsheng Ren^a, Hungjen Hsu^a, Ruihe Li^a, Xuning Feng^{a,b}, Dongxu Guo^{a,c},
Xuebing Han^a, Languang Lu^a, Xiangming He^{a,b}, Shang Gao^a, Junxian Hou^a, Yan Li^a,
Yongling Wang^a, Minggao Ouyang^{a,*}

^a State Key Laboratory of Automotive Safety and Energy, Tsinghua University, Beijing, 100084, China

^b Institute of Nuclear and New Energy Technology, Tsinghua University, Beijing, 100084, China

^c Department of Automation, Tsinghua University, Beijing, 100084, China

ARTICLE INFO

Article history:

Received 8 November 2019

Received in revised form

12 November 2019

Accepted 13 November 2019

Available online 20 November 2019

Keywords:

Lithium-ion battery

Battery safety

Thermal runaway

Battery aging

Lithium plating

ABSTRACT

Thermal runaway is a major concern for the large-scale application of lithium-ion batteries. The thermal runaway performance of lithium-ion batteries not only depends on materials and cell design, but also changes with degradation. This paper presents a comparative investigation of the aging effects on the thermal runaway behavior of a large format lithium-ion battery. The batteries are first degraded under four different aging paths. The aging mechanisms are then investigated through post-mortem analysis on the battery at the end of life, by comparing the electrochemical properties, morphology and composition of the fresh and degraded electrodes. The thermal stabilities of the fresh and degraded electrodes are also evaluated using differential scanning calorimetry. Adiabatic thermal runaway tests are performed on the batteries at different states of health using accelerating rate calorimetry to reveal the evolution of battery thermal runaway performance under the four degradation paths. Finally, the correlations between the aging mechanism and the changes in battery thermal runaway behavior are summarized. The results show that the thermal stability of the anode+electrolyte thermodynamic system exhibits obvious changes, which contribute to the evolution of battery thermal runaway performance, while the thermal stability of the cathode remained unchanged. Lithium plating turns out to be the key reason for the deterioration of battery thermal runaway performance during aging process.

© 2019 Elsevier B.V. All rights reserved.

1. Introduction

Lithium-ion batteries are the most promising electrochemical energy storage system for electric vehicles (EVs), due to their high energy density and prolonged cycle life. However, safety accidents associated with thermal runaway (TR) of lithium-ion batteries have occurred occasionally, hindering the development of EVs [1–3]. The safety performance of lithium-ion batteries is still of great concern, and will become more critical in the large-scale application of high-energy-density lithium-ion batteries [1]. Therefore, efforts are urgently required to understand battery TR mechanism and develop safer batteries.

Generally, the cathode, anode and electrolyte of lithium-ion

batteries should operate within their safe and reliable temperature windows [4]. Once the temperature exceeds the safe temperature windows, exothermic reactions between battery components begin, thus resulting in an abnormal increase in battery temperature and further exothermic reactions. The whole process is known as the heat-temperature-reaction (HTR) loop [1,5]. The HTR loop is a self-accelerated process with a large amount of heat generation, leading the battery to TR. The TR performance of lithium-ion batteries can be evaluated by three critical temperatures $\{T_1, T_2, T_3\}$, which represent the onset temperature of self-heating, the onset temperature of TR and the maximum temperature, respectively [6]. Higher T_1 and T_2 indicate that the tested battery is more thermally stable, while a lower T_3 manifests less heat generation during the TR process.

The exothermic reactions during the HTR loop of lithium-ion batteries have been investigated through tests on materials and batteries using differential scanning calorimetry (DSC) [7,8] and

* Corresponding author.

E-mail addresses: rds14@mails.tsinghua.edu.cn (D. Ren), ouymg@tsinghua.edu.cn (M. Ouyang).

accelerating rate calorimetry (ARC) [9,10]. When battery temperature rises up to T_1 (around 70–90 °C), the solid electrolyte interface (SEI) film on anode surface decomposes and generates significant amount of heat, resulting in self-heating of the battery [11,12]. The lithiated graphite begins to react with the electrolyte at around 120–140 °C, once the SEI film is seriously damaged and cannot protect the anode from contacting with electrolyte [13–15]. The lithiated graphite also reacts with the binder as battery temperature increases [16,17]. The layered-structure cathode material, such as $\text{LiNi}_x\text{Co}_y\text{Mn}_z\text{O}_2$, starts to decompose at around 200 °C, generating a significant amount of oxygen [18–21]. The released oxygen can oxidize the electrolyte [22–24] or even react with the lithiated graphite [6,8,25–27], generating large amount of heat and bringing the battery temperature to T_2 . Finally, TR occurs, and the battery temperature reaches T_3 .

Safe operation of lithium-ion batteries at the begin of life (BoL) can be ensured through chemistry design and battery management system [4] based on the in-depth understanding of the TR mechanism. However, the TR performance of lithium-ion batteries changes during the aging process [10,28–30], bringing new safety risks. According to the Lithium-ion Power Battery Safety Research Report (2019) [2] by the Battery Safety Laboratory at Tsinghua University, safety accidents of EVs in China usually happened in the vehicles after around one year operation. As a result, it is important to investigate the aging effects on the battery TR performance to guarantee the safe operation of lithium-ion batteries during whole life cycle.

The changes in the battery TR performance during the aging process are strongly dependent on the degradation paths, aging mechanism and battery chemistries [29,31–33]. Some researchers found that batteries degraded under high-temperature storage showed improved thermal stability with increased T_1 and lower temperature rate [10,28,34,35]. Batteries that experienced longer high-temperature storage would exhibit higher T_1 and lower self-heating rate [36]. The changes in the battery TR performance after cycling at room temperature or at high temperature varied with battery chemistries and operating parameters. Some researchers found that batteries showed lower T_1 and T_2 and slightly increased self-heating rate after cycling at room temperature or high temperature, indicating the decay of battery thermal stability [32,37]. In contrast, Roth et al. [10,28] and Börner et al. [29] observed improved battery TR performance after high-temperature cycling. For the batteries cycled at low temperature, dramatic deterioration of battery thermal stability with decreased T_1 and T_2 and increased self-heating rate has been observed by several researchers [31,32,38–40]. Friesen et al. [39] found that the battery cycled at 0 °C/1C exhibited a decreased T_1 to less than 50 °C and a new exothermic peak between 30 °C and 120 °C during adiabatic TR tests. Waldmann et al. [40] also observed an obvious decrease in T_1 and T_2 for the batteries cycled at 0 °C/0.5C. Lithium plating on the anode surface was identified as the root cause for the deterioration of battery TR performance after low-temperature cycling [39–43].

According to the existing literature, the changes in battery TR behavior during the aging process depends strongly on the degradation history and mechanisms. However, current research mainly focuses on the changes in battery TR behavior under only one or two specific aging conditions. The correlations between aging mechanism and changes in battery TR performance have not been well established. Therefore, comprehensive studies are further required to elucidate the aging effects on battery safety under various operating conditions.

In this paper, the aging effects on the TR behavior of a large format lithium-ion battery are investigated in detail. A series of TR tests on the batteries degraded under four different aging paths are carried out using extended volume ARC (EV-ARC). The correlations

between the aging mechanism and the changes in battery TR behavior are revealed from post-mortem analysis on the degraded electrodes. The results presented in this paper give a comprehensive understanding of the effects of various side reactions on battery TR performance, and provide guidance for the safety management of lithium-ion batteries during whole life cycle.

2. Experiments

2.1. Battery aging tests

A commercial pouch lithium-ion battery with a 24Ah nominal capacity was investigated in this study. The battery had $\text{Li}_x(\text{Ni-CoMn})_{1/3}\text{O}_2$ (NCM) cathode and graphite anode, and the separator was polyethylene-based separator with ceramic coating.

Four accelerating aging tests were designed to investigate the effects of low-temperature cycling, fast-charging cycling, high-temperature cycling and high-temperature storage on battery TR behavior, as presented in Table 1.

Prior to the aging tests, a reference performance test (RPT) was conducted on the tested batteries at 25 °C to measure the battery capacities. In the RPT, the batteries were cycled three times at 0.33C under the following procedures: 1) constant current (CC) charge to 4.2 V at 0.33C and then constant voltage (CV) charge at 4.2 V until current reduced to <0.05C; 2) rest for 30min; 3) discharge to 2.5 V at 0.33C; 4) rest for 30 min. The discharge capacity in the third cycle was determined as the capacity of the tested battery. RPTs were also carried out during the accelerating aging tests to characterize the evolution of the battery capacity, as indicated in Table 1. The state of health (SOH) was defined by Eqn. (1), where Q was the discharge capacity, and Q_0 was the initial capacity of the tested battery. The batteries were tested using several 8-channel battery cyclers (Neware BTS4000-5V100A). Environmental chambers (DONGGUAN BELL BE-TH-150M3) were utilized to control the battery temperature.

$$\text{SOH} = \frac{Q}{Q_0} \times 100\% \quad (1)$$

Seventeen batteries were tested in parallel for each kinds of aging test. Sixteen of them were stopped in sequence at around 95%, 90%, 85%, and 80% SOH (4 batteries for each SOH) for TR tests. The remaining battery was degraded to the end of life (EoL, 80% SOH) and was subsequently disassembled for post-mortem analysis.

2.2. Electrochemical impedance spectroscopy (EIS) Test

EIS tests were performed on the batteries at the BoL and EoL to investigate the changes in battery impedance. The batteries were fully charged to 4.2 V at 0.33C by the CCCV charging protocol prior to the EIS tests. The battery impedance was then measured at 25 °C using an Autolab modular potentiostat/galvanostat (PGSTAT302N, Metrohm, Switzerland) in potentiostatic mode. The amplitude of the perturbation was set as 5 mV over the frequency range between 0.01 and 5 kHz.

2.3. Cell opening and coin cells fabrication

The degraded batteries were dismantled at fully-charged state in an argon filled glove box after the EIS tests. Coin cells were assembled using the harvested electrodes paired with lithium metal counter electrodes. The coin cells were tested with a current density of 0.088 mA·cm² (around 1/30C) at 25 °C. The NCM/Li coin cells were first discharged to 2.8 V to obtain initial lithiation capacities, while the graphite/Li coin cells were charged to 2.0 V to

Table 1
Accelerating aging tests.

No.	Degradation path	Test procedures
1	Cycling at -5 °C/1C	A. Cycling procedure at -5 °C 1) CC(1C)-CV charge to 4.2 V until current < 0.05C 2) CC(1C) discharge to 2.5 V 3) Rest for 30 min between charge and discharge B. RPT at 25 °C every 10 cycles
2	Cycling at 25 °C/2C	A. Cycling procedure at 25 °C 1) CC(2C)-CV charge to 4.2 V until current < 0.05C 2) CC(2C) discharge to 2.5 V 3) Rest for 30 min between charge and discharge B. RPT at 25 °C every 240 cycles
3	Cycling at 55 °C/1C	A. Cycling procedure at 55 °C 1) CC(1C)-CV charge to 4.2 V until current < 0.05C 2) CC(1C) discharge to 2.5 V 3) Rest for 30 min between charge and discharge B. RPT at 25 °C every 120 cycles
4	Storage at 55 °C/100%SOC	A. CC(0.33C)-CV charge to 4.2 V until current < 0.05C at 25 °C B. Storage at 55 °C C. RPT at 25 °C every 15 days

measure initial delithiation capacities. The coin cells were then cycled three times to measure their capacities. The voltage range for NCM/Li coin cells was 2.8–4.3 V, while that for graphite/Li coin cells was 0.01–2.0 V.

2.4. Morphology and composition characterization

Scanning electron microscopy (SEM) and X-ray photoelectron spectroscopy (XPS) analysis were conducted to characterize the morphology and composition change of the degraded electrodes. The electrodes used for SEM and XPS analyses were harvested from the lithiated NCM/Li coin cells and delithiated graphite/Li coin cells rather than the fully-charged batteries. That helps to retard the reactions between the tested samples and air when conducting those experiments. The NCM/Li coin cells were lithiated to 2.8 V, while the graphite/Li coin cells were delithiated to 2.0 V. SEM analysis was conducted with a Zeiss Merlin field emission scanning electron microscope. XPS characterization was performed with a ThermoFisher Scientific ESCALAB 250Xi X-ray photoelectron spectrometer microprobe. The X-ray spot diameter was set to 500 μm . The XPS results were calibrated with a C1s emission peak of 284.6 eV and analyzed by XPSPEAK. Inductively coupled plasma optical emission spectrometry (ICP-OES) was further conducted on the harvested anodes to measure the amount of dissolved transition metal on the anode surface, using a IRIS Intrepid II ICP-OES by ThermoFisher Scientific.

Moreover, ^7Li solid state magic-angle spinning nuclear magnetic resonance (MAS-NMR) was conducted on the fully-charged anodes to detect possible plated lithium on the anode. The NMR tests samples were prepared in the glove box by packing the powdered anodes (around 50 mg) into 3.2 mm rotors. The NMR equipment was JNM-ECA600 by JEOL. The Larmor frequency was set to 232.76 MHz, and the length of a single pulse sequence was 1.6 μs with the pulse delay of 20 s. The ^7Li solid state MAS-NMR spectra were recorded at a frequency of 15 kHz within the spectrum range of -500 to +500 ppm, and the number of scans was 16. The chemical shifts were referenced to LiCl powder.

2.5. DSC tests

DSC tests were carried out to investigate the thermal stability of electrode materials using a DSC 214 Polyma (NETZSCH, Germany). The DSC tests were conducted in a nitrogen atmosphere with the gas flow rate set as 40 $\text{mL} \cdot \text{min}^{-1}$. The electrode materials for DSC

tests were obtained in the fully-charged state harvested in Sec. 2.3. Prior to the DSC tests, the electrodes were soaked in dimethyl carbonate (DMC) for 2 h and dried in glove box for 2 more hours to remove the residual lithium salt (LiPF_6). DSC samples were prepared using electrode materials that were scratched off from the current collectors. The electrolyte (1.0M LiPF_6 in DMC: ethyl methyl carbonate (EMC): ethylene carbonate (EC) (1:1:1 in volume)) was refilled into the crucible. According to our previous study [8], anode+electrolyte and cathode+anode are the two dominating exothermic reaction pairs during the battery TR process. Thus, three kinds of samples with different compositions were prepared for DSC tests, as presented in Table 2. The mass ratios of the cathode, anode and electrolyte were maintained as the same as those in the 24Ah battery. During the DSC tests, the samples were heated from room temperature to 600 °C at a heating rate of 20 °C $\cdot \text{min}^{-1}$. The test results of sample anode+electrolyte and cathode+anode can help to explain the evolution of battery TR behavior, whereas those of cathode material can reveal the change in its thermal stability.

2.6. Thermal runaway tests

Adiabatic TR tests were performed on batteries at different SOH to investigate the changes in battery TR behavior, as summarized in Table 3. An EV-ARC manufactured by Thermal Hazard Technology was utilized for TR tests. Two batteries at the same aging state were connected in parallel and tested in each TR test, as presented in our previous paper [8]. The two batteries were wrapped by high temperature insulation Kapton tape to keep compact contact during the TR test. A K type thermocouple was inserted between the two batteries to measure the internal temperature, which was used to evaluate the battery TR performance. During the TR tests, the EV-ARC was operated under the heat-wait-see mode. The start temperature was set at 40 °C with a temperature step of 5 °C, and the wait time and seek time were 30 min and 20 min, respectively. The temperature rate sensitivity was 0.01 °C $\cdot \text{min}^{-1}$, meaning that the EV-ARC system would go into the exotherm mode to track the temperature rise of tested batteries and maintain the adiabatic

Table 2
Samples for DSC tests.

Sample no.	Composition	Mass
1	anode+electrolyte	3.4 mg + 3 mg
2	cathode+anode	6 mg + 3.4 mg
3	cathode	6 mg

Table 3
Summary of TR tests.

Degradation path	Battery SOH	Test counts
Fresh	100%	$1 \times 2 = 2$
Cycling at $-5^\circ\text{C}/1\text{C}$	95%, 90%, 85%, 80%	$4 \times 2 = 8$
Cycling at $25^\circ\text{C}/2\text{C}$	95%, 90%, 85%, 80%	$4 \times 2 = 8$
Cycling at $55^\circ\text{C}/1\text{C}$	95%, 90%, 85%, 80%	$4 \times 2 = 8$
Storage at $55^\circ\text{C}/100\%\text{SOC}$	95%, 90%, 85%, 80%	$4 \times 2 = 8$

condition if the measured temperature rate exceeded $0.01^\circ\text{C} \cdot \text{min}^{-1}$.

3. Results and discussion

3.1. Battery degradation behavior

The capacity degradation behavior of the 24Ah battery under different aging paths is presented in Fig. 1. As showed in Fig. 1(a), the batteries cycled at -5°C exhibited rapid degradation and reached EoL after only 60 cycles, whereas the batteries cycled at higher temperatures exhibited better performance, with the cycle numbers reaching 2820 and 1020 at 25°C and 55°C , respectively. The batteries stored at $55^\circ\text{C}/100\%\text{SOC}$ can last 195 days until EoL was reached.

The impedance profiles of the batteries at the BoL and EoL are compared in Fig. 2. The ohmic resistance of the tested battery can be evaluated by the interception at $-Z_{\text{imag}} = 0$, while the total diameter of all the semicircles represents the charge transfer resistance. All the degraded batteries exhibited increased impedance. The battery cycled at $-5^\circ\text{C}/1\text{C}$ showed a slight increase of charge transfer resistance, while the ohmic resistance remained unchanged. For the battery stored at $55^\circ\text{C}/100\%\text{SOC}$, the ohmic resistance rose to nearly twice that of the fresh battery (from 0.87 to 1.75 mΩ), while the charge transfer resistance exhibited only a minor increment. The batteries cycled at $25^\circ\text{C}/2\text{C}$ and $55^\circ\text{C}/1\text{C}$ showed significant increases in ohmic and charge transfer resistances, especially for the battery cycled at $25^\circ\text{C}/2\text{C}$, which charge transfer resistance increased fivefold compared to that of the fresh battery.

After EIS tests, the fresh and degraded batteries were disassembled at fully-charged state in the glove box. Electrode materials were harvested and analyzed in detail to reveal the aging mechanism.

The fully-charged anodes harvested from batteries at the BoL and EoL are presented in Fig. 3. The cathodes are not presented here since there were little differences in appearance between the fresh

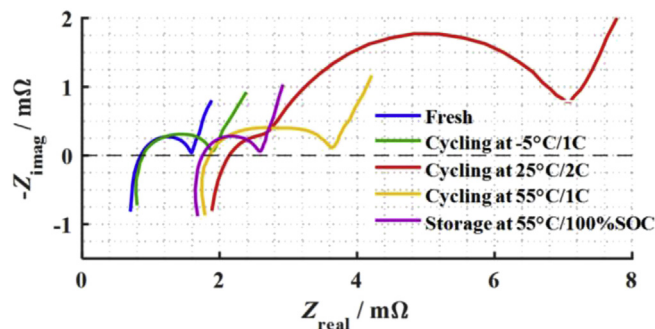


Fig. 2. Impedance profiles of the batteries at the BoL and EoL under different degradation paths.

and degraded cathodes. As shown in Fig. 3(a), the fresh anode exhibited a uniform golden color with no obvious deposits on the surface. The appearance of the anodes cycled at $55^\circ\text{C}/1\text{C}$ and stored at $55^\circ\text{C}/100\%\text{SOC}$ were similar to that of the fresh anode with only minor changes in color and a few deposits, whereas the anodes cycled at $-5^\circ\text{C}/1\text{C}$ and $25^\circ\text{C}/2\text{C}$ showed significant changes. Large amount of lithium metal was deposited on the anode cycled at $-5^\circ\text{C}/1\text{C}$, turning its color into gray, as shown in Fig. 3(b). The anode cycled at $25^\circ\text{C}/2\text{C}$ exhibited heterogeneous degradation behavior. The central of the anode remained golden, while the edge changed to black, indicating different lithiation degrees. Furthermore, drying out of electrolyte was observed when disassembling the battery cycled at $25^\circ\text{C}/2\text{C}$, indicating consumption of electrolyte during the aging process. Electrolyte consumption will lead to a sharp increase of battery impedance, which is consistent with the drastic growth in both ohmic and charge transfer resistance for the battery cycled at $25^\circ\text{C}/2\text{C}$ in Fig. 2.

Coin cells were fabricated with electrodes from fresh and degraded batteries to characterize the degradation mode under different aging paths. The results are presented in Table 4. $C_{p,\text{Li}}$ and C_p represent the first (from the initial state to 2.8 V) and total (from 4.3 to 2.8 V) lithiation capacity of the cathode, respectively. $y_0 = 1 - C_{p,\text{Li}}/C_p$ is calculated to evaluate the lithiation degree of cathode. Similarly, $C_{n,\text{deli}}$ and C_n denote the first (from the initial state to 2.0 V) and total (from 0.01 to 2.0 V) delithiation capacity of the anode, respectively. $x_0 = C_{n,\text{deli}}/C_n$ represents the lithiation degree of anode. The decreases of C_p and C_n indicate loss of active material (LAM) at the cathode and anode, respectively, while the changes in y_0 and x_0 reflect loss of lithium inventory (LLI) [44–47].

For the battery cycled at $-5^\circ\text{C}/1\text{C}$, C_n decreased slightly, indicating LAM at anode, while cathode showed no LAM, as C_p

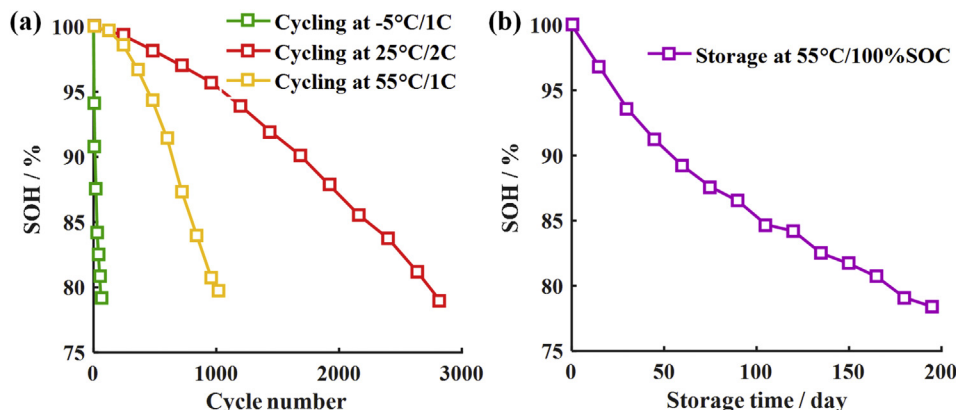


Fig. 1. Degradation behavior of the tested battery under different aging paths. (a) cycling at $-5^\circ\text{C}/1\text{C}$, $25^\circ\text{C}/2\text{C}$ and $55^\circ\text{C}/1\text{C}$; (b) storage at $55^\circ\text{C}/100\%\text{SOC}$.

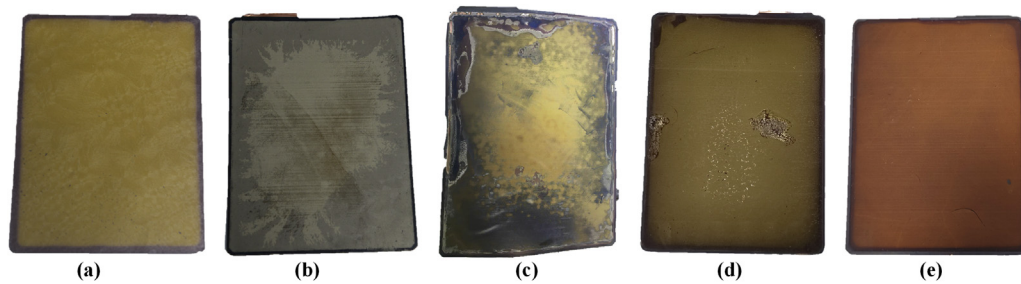


Fig. 3. Photographs of the fully-charged anodes harvested from batteries at the BoL and EoL under different degradation paths. (a) fresh; (b) cycling at $-5\text{ }^{\circ}\text{C}/1\text{C}$; (c) cycling at $25\text{ }^{\circ}\text{C}/2\text{C}$; (d) cycling at $55\text{ }^{\circ}\text{C}/1\text{C}$; (e) storage at $55\text{ }^{\circ}\text{C}/100\%\text{SOC}$.

Table 4

Summary of coin cells tests results.

Degradation path	Cathode			Anode		
	$C_{p,li}/\text{mAh}$	C_p/mAh	y_0	$C_{n,deli}/\text{mAh}$	C_n/mAh	x_0
Fresh	3.197	3.625	0.118	3.085	3.704	0.833
Cycling at $-5\text{ }^{\circ}\text{C}/1\text{C}$	2.994	3.624	0.174	2.386	3.567	0.669
Cycling at $25\text{ }^{\circ}\text{C}/2\text{C}$	3.079	3.417	0.099	2.659	3.263	0.815
Cycling at $55\text{ }^{\circ}\text{C}/1\text{C}$	2.908	3.462	0.160	2.690	3.480	0.773
Storage at $55\text{ }^{\circ}\text{C}/100\%\text{SOC}$	2.948	3.501	0.158	2.536	3.692	0.687

remained nearly unchanged. Moreover, x_0 exhibited a significant decline, demonstrating severe LLI inside the battery cycled at $-5\text{ }^{\circ}\text{C}/1\text{C}$. The battery cycled at $25\text{ }^{\circ}\text{C}/2\text{C}$ suffered from LAM at both cathode and anode, but it underwent little LLI, as C_p and C_n declined obviously, while y_0 and x_0 remained nearly unchanged. Likewise, LAM at cathode and anode occurred in the battery cycled at $55\text{ }^{\circ}\text{C}/1\text{C}$, which was demonstrated by the decline of C_p and C_n . The battery also experienced minor LLI, as x_0 decreased slightly and y_0 increased. The battery stored at $55\text{ }^{\circ}\text{C}$ exhibited significant LLI and minor LAM at cathode, indicated by the changes in y_0 and C_p , respectively.

3.2. Aging mechanism identification

SEM, XPS, ICP-OES, and NMR tests were conducted on the electrode materials to identify the battery aging mechanism under different degradation paths.

The SEM images of fresh and degraded cathodes are presented in Fig. 4. The cathode cycled at $-5\text{ }^{\circ}\text{C}/1\text{C}$ exhibited the same morphology as that of the fresh cathode with the particles remaining intact. However, secondary particle cracking was observed in the cathodes cycled at $25\text{ }^{\circ}\text{C}/2\text{C}$ and $55\text{ }^{\circ}\text{C}/1\text{C}$, manifesting LAM at cathode [48]. This is consistent with the results presented in Table 4. Deposits were observed on the surface of the cathode stored at $55\text{ }^{\circ}\text{C}/100\%\text{SOC}$, resulting from oxidation of electrolyte on cathode surface under high potential and temperature [49]. Deposits on the cathode surface will further lead to pore clogging and thus LAM at cathode [50], which is also consistent with the results in Table 4.

Fig. 5 presents XPS spectra of the fresh and degraded cathodes. Four peaks appear in the C1s spectra at binding energies of 284.8 eV, 286.8 eV, 288.5 eV, and 290.1 eV, representing the C–C/C–H, C–O, C=O, and CO_3 species, respectively [51,52]. The O1s spectra exhibit three peaks at 529.5 eV, 532.0 eV and 533.4 eV, corresponding to the M(metal oxide)–O, CO_3 , and C–O species, respectively [51,52]. The F1s spectra shows two peaks at 685.2 eV and 687.1 eV, which correspond to LiF and P–F species, respectively [51,52].

For the cathode cycled at $-5\text{ }^{\circ}\text{C}/1\text{C}$, the peak related to M–O

species in the O1s spectra remained unchanged, indicating that no obvious growth of cathode electrolyte interphase (CEI) film occurred on the cathode surface. In contrast, the cathodes degraded under the other three aging paths all showed remarkable formation of CEI film with M–O peak in the O1s spectra apparently declining. For the cathode cycled at $25\text{ }^{\circ}\text{C}/2\text{C}$ and $55\text{ }^{\circ}\text{C}/1\text{C}$, the C–O and CO_3 peaks in the C1s spectra showed enhanced intensity, while the LiF peak in the F1s spectra weakened. That indicates that CEI film on those two cathodes were mainly composed of Li_2CO_3 , ROCO_2Li , and $\text{R-CH}_2\text{-O-CO}_2\text{Li}$. The cathode degraded at $55\text{ }^{\circ}\text{C}/100\%\text{SOC}$ showed an obvious increase in LiF species in the F1s spectra and a decline of C–O and CO_3 species in the C1s spectra, demonstrating that LiF was the dominant component of CEI film on that cathode.

Fig. 6 displays the SEM images of the fresh and degraded anodes, and XPS spectra of the anodes are presented in Fig. 7. All the degraded anodes showed significant changes in morphology. As shown in Fig. 6(b), the anode cycled at $-5\text{ }^{\circ}\text{C}/1\text{C}$ showed thick deposits on the electrode surface, and the graphite particles were invisible due to the reaction between plated lithium and electrolyte. Lithium plating was prone to occur on the anode surface during low-temperature charging, resulting in LLI [41,43]. The plated lithium reacted with electrolyte to form Li_2CO_3 [53], validated by the XPS results in Fig. 7. Compared to the fresh anode, the anode cycled at $-5\text{ }^{\circ}\text{C}/1\text{C}$ exhibited an increased in CO_3 peak in the C1s spectra and a weakened C–O peak in the O1s spectra. As shown in Fig. 6(c)–(e), the anodes degraded under the other three paths also showed thick deposits on the surface and pore clogging, resulting from SEI film thickening and electrolyte decomposition on the anode surface [50]. Thickening of the SEI film consumes lithium inventory and hence leads to LLI [46], while pore clogging results in an increment in the anode impedance and LAM at anode, which is consistent with the results in Fig. 2 and Table 4. The composition of the SEI film on the anode surface were analyzed by XPS. As presented in Fig. 7, the anode cycled at $25\text{ }^{\circ}\text{C}/2\text{C}$ showed enhanced peaks at 289.9 eV and 286.8 eV in the C1s spectra, indicating the increases of CO_3 species (Li_2CO_3 , ROCO_2Li) and C–O species ($\text{R-CH}_2\text{-O-CO}_2\text{Li}$), respectively. For the anodes cycled at $55\text{ }^{\circ}\text{C}/1\text{C}$ and stored at $55\text{ }^{\circ}\text{C}/100\%\text{SOC}$, an increase of C–O species ($\text{R-CH}_2\text{-O-CO}_2\text{Li}$) was observed from the changes in the C1s spectra.

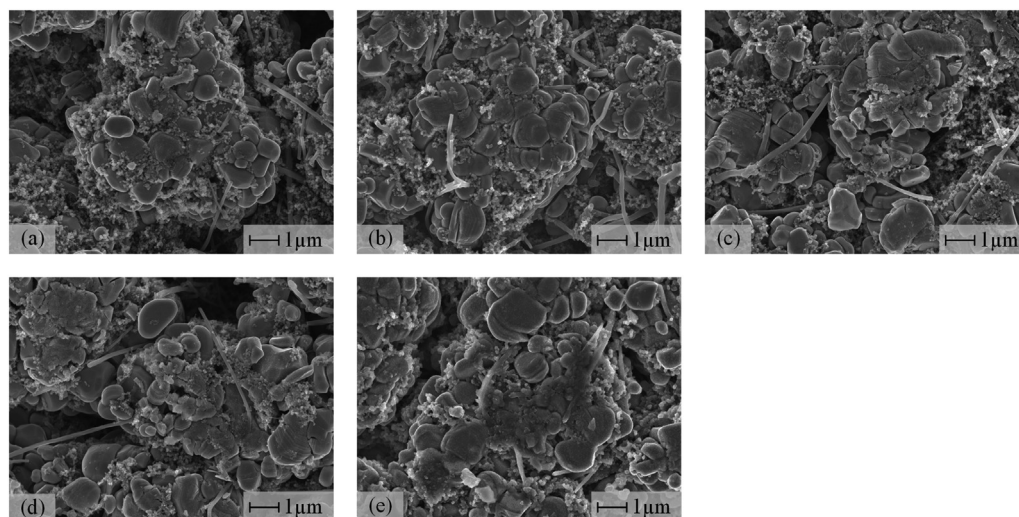


Fig. 4. SEM images of the cathodes at the BoL and EoL under different degradation paths. (a) fresh; (b) cycling at $-5\text{ }^{\circ}\text{C}/1\text{C}$; (c) cycling at $25\text{ }^{\circ}\text{C}/2\text{C}$; (d) cycling at $55\text{ }^{\circ}\text{C}/1\text{C}$; (e) storage at $55\text{ }^{\circ}\text{C}/100\%\text{SOC}$.

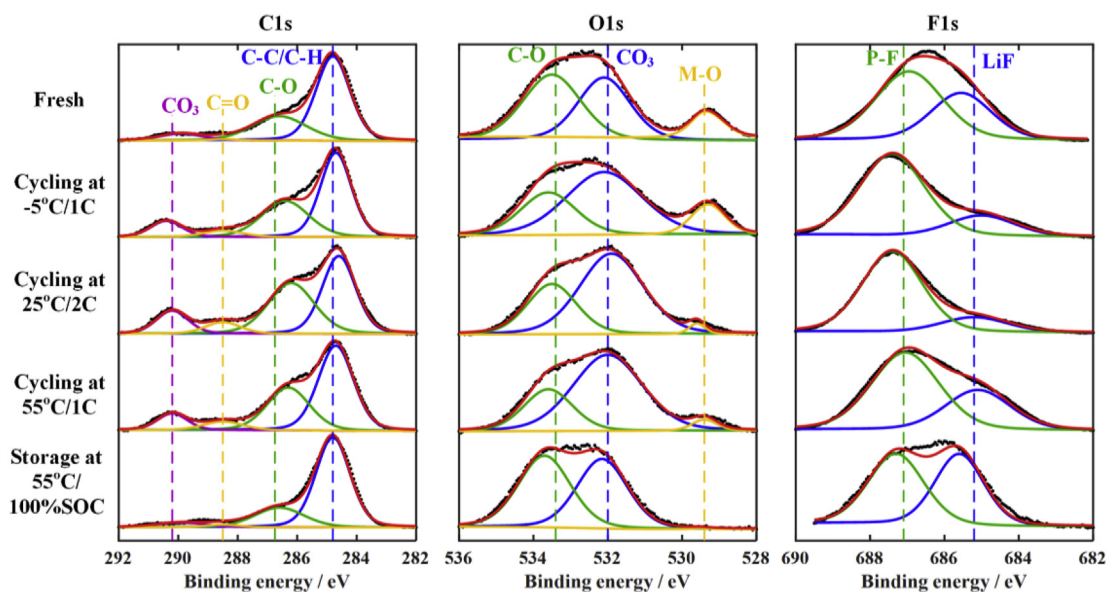


Fig. 5. XPS spectra of the cathodes at the BoL and EoL under different degradation paths.

Moreover, all the degraded anodes exhibited enhanced peak intensity at 685.2 eV (LiF) but weakened peak intensity at 687.1 eV (PVDF), implying massive deposits on the anodes surface and generation of LiF due to SEI film thickening, which is consistent with the change in morphology seen in the SEM images in Fig. 6.

Table 5 presents the ICP-OES results of the anodes. The anode cycled at $25\text{ }^{\circ}\text{C}/2\text{C}$ and stored at $55\text{ }^{\circ}\text{C}/100\%\text{SOC}$ experienced obvious increase of Mn content due to transition metal dissolution [54], while the anodes at $-5\text{ }^{\circ}\text{C}/1\text{C}$ and $55\text{ }^{\circ}\text{C}/1\text{C}$ only showed minor changes in the concentration of transition metal. The transition metal ions dissolved in the cathode were prone to pass through the separator and deposit on the anode surface, resulting in accelerated growth of the SEI film [55].

^7Li solid state MAS-NMR were performed on the anodes to detect plated lithium metal, as shown in Fig. 8. The fresh anode exhibited two peaks at chemical shifts of 3.0 and 48.0 ppm , corresponding to Li_xC_6 and the SEI film, respectively [56,57]. The anode

cycled at $-5\text{ }^{\circ}\text{C}/1\text{C}$ showed an intense peak of lithium metal at 268.5 ppm , indicating severe lithium plating [56,57]. The anode cycled at $25\text{ }^{\circ}\text{C}/2\text{C}$ also experienced slight lithium plating, as a minor peak appeared at 268.5 ppm in the NMR spectrum. The NMR spectra of the anodes cycled at $55\text{ }^{\circ}\text{C}/1\text{C}$ and stored at $55\text{ }^{\circ}\text{C}/100\%\text{SOC}$ both showed no signal for lithium metal, demonstrating no plated lithium on the two anodes.

The battery degradation mechanisms under the four aging paths can be summarized in Table 6 based on the post-mortem analysis results. The batteries cycled at $-5\text{ }^{\circ}\text{C}/1\text{C}$ suffered from LLI, LAM at anode and a slightly increase in the ohmic resistance. Lithium plating on the anode was the dominant side reaction during low-temperature cycling. The degradation mode of the batteries cycled at $25\text{ }^{\circ}\text{C}/2\text{C}$ was LAM at cathode and anode, and significant impedance increment. The cathode experienced secondary particle cracking, CEI film formation and transition metal dissolution, while the anode suffered from SEI film thickening and slightly lithium

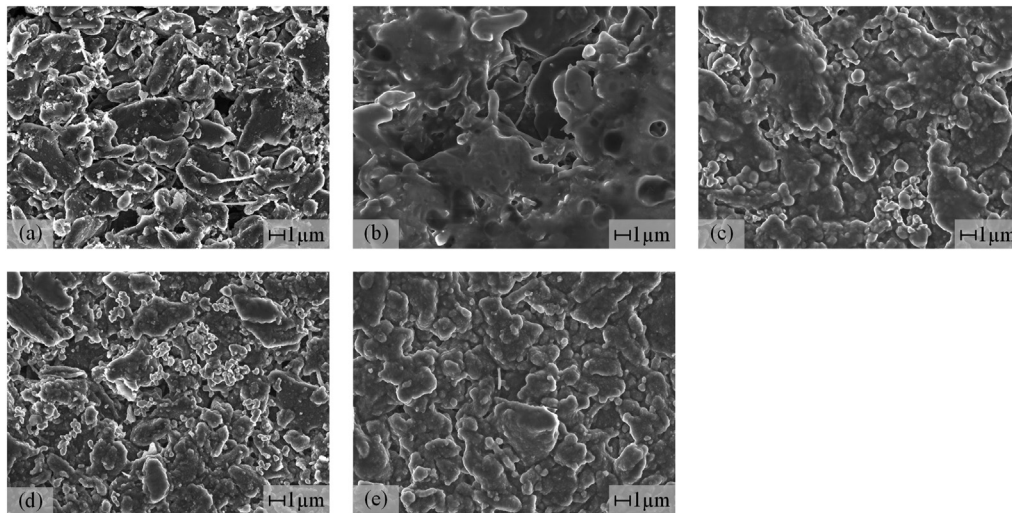


Fig. 6. SEM images of the anodes at the BoL and EoL under different degradation paths. (a) fresh; (b) cycling at $-5\text{ }^{\circ}\text{C}/1\text{C}$; (c) cycling at $25\text{ }^{\circ}\text{C}/2\text{C}$; (d) cycling at $55\text{ }^{\circ}\text{C}/1\text{C}$; (e) storage at $55\text{ }^{\circ}\text{C}/100\%\text{SOC}$.

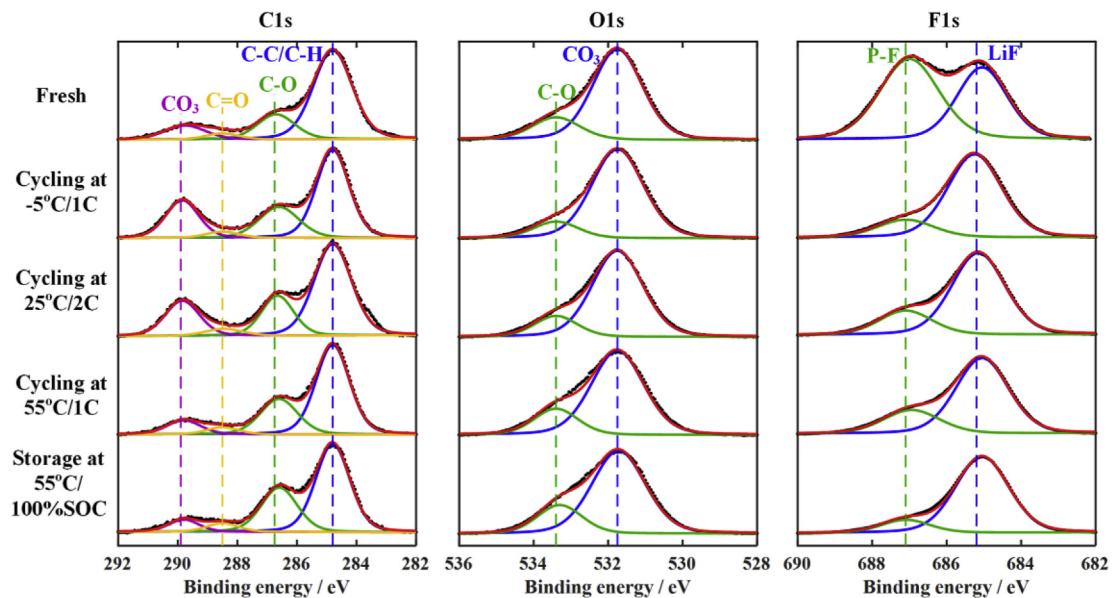


Fig. 7. XPS spectra of the anodes at the BoL and EoL under different degradation paths.

Table 5

ICP-OES results of the anodes at the BoL and EoL under different degradation paths.

Degradation path	Element content/ppm		
	Mn	Co	Ni
Fresh	88.37	49.59	98.29
Cycling at $-5\text{ }^{\circ}\text{C}/1\text{C}$	53.92	43.59	58.95
Cycling at $25\text{ }^{\circ}\text{C}/2\text{C}$	675.4	129.2	198.2
Cycling at $55\text{ }^{\circ}\text{C}/1\text{C}$	149.0	34.88	52.07
Storage at $55\text{ }^{\circ}\text{C}/100\%\text{SOC}$	494.8	109.9	126.46

plating. Electrolyte consumption also happened to the batteries cycled at $25\text{ }^{\circ}\text{C}/2\text{C}$, resulting in impedance increment. For the batteries cycled at $55\text{ }^{\circ}\text{C}/1\text{C}$, LAM at cathode and anode and impedance increment were the dominant aging mechanism. LAM at cathode was induced by secondary particle cracking and CEI film formation. The anode underwent SEI film thickening, which also

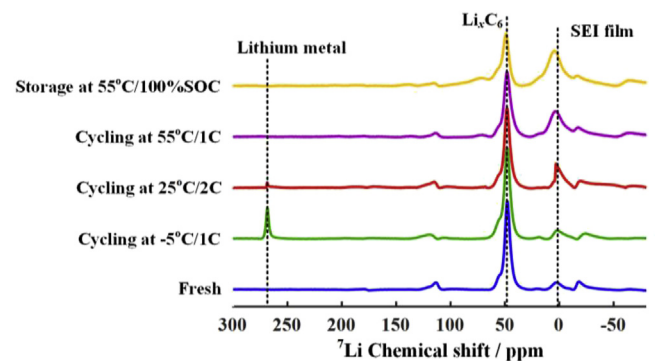


Fig. 8. ^7Li solid state MAS-NMR spectra of the anodes at the BoL and EoL under different degradation paths.

Table 6
Summary of battery aging mechanisms under the four degradation paths.

Degradation path	Degradation mode	Side reactions
Cycling at -5 °C/1C	LLI, LAM at anode, increase of ohmic resistance	Lithium plating
Cycling at 25 °C/2C	LAM at cathode and anode, increase of ohmic and charge transfer resistance	Cathode: secondary particle cracking, CEI film formation and transition metal dissolution Anode: SEI film thickening and slightly lithium plating
Cycling at 55 °C/1C	LLI, LAM at cathode and anode, increase of ohmic and charge transfer resistance	Electrolyte consumption Cathode: secondary particle cracking and CEI film formation Anode: SEI film thickening
Storage at 55 °C/100% SOC	LLI, LAM at cathode, increase of ohmic resistance.	Cathode: CEI film formation and transition metal dissolution Anode: SEI film thickening

led to minor LLI. The batteries stored at 55 °C/100%SOC experienced severe LLI, LAM at cathode and increase of ohmic resistance. LLI was caused by SEI film thickening in the anode, which also contributed to impedance increment. The cathode suffered from CEI film formation and transition metal dissolution.

3.3. Thermal stability of the electrodes

DSC tests results of the fresh and degraded electrodes are compared in Fig. 9 and Fig. 10. The heat flow values in Figs. 9 and Fig. 10 are normalized by the mass of solid electrode materials (i.e. the mass of the cathode, anode, or the total mass of the cathode and anode) in the tested samples. The heat generation of tested samples normalized by the mass of electrodes is presented in Table 7.

For the batteries cycled at -5 °C/1C, a new exothermic peak between 100 °C and 180 °C appeared in the DSC profile of sample anode+electrolyte, as shown in Fig. 9. The heat generation of the new exothermic peak reached 280.1 J g⁻¹, accounting for 11.4% of the total heat generation (2457.0 J g⁻¹). The exothermic peak was caused by the reaction between electrolyte and plated lithium on the anode surface [29]. As presented in Sec. 3.2, large amount of lithium metal was deposited on the anode cycled at -5 °C/1C. The deposited lithium metal is more reactive than lithiated graphite and reacts with electrolyte at lower temperature, resulting in a large amount of heat generation and thus the new exothermic peak in the DSC profile [29]. The anode cycled at 25 °C/2C began to react with the electrolyte at a slightly lower temperature than the fresh anode, caused by the minor plated lithium on the anode. For the battery cycled at 55 °C/1C, the DSC profile and heat generation of sample anode+electrolyte were nearly the same as those of the fresh anode except for the minor difference in the exothermic peak

intensity at around 250 °C. Compared to the fresh, the anode cycled at 55 °C/1C exhibited similar lithiation degree but thickened SEI film, which would lead to increment in the heat generation from SEI film decomposition and thus increased intensity of the peak at 250 °C. As shown in Fig. 9, the exothermic reactions between electrolyte and the anode stored at 55 °C/100%SOC were postponed compared to those of the fresh anode. Moreover, the exothermic peak at about 350 °C disappeared in the DSC profile of the sample anode+electrolyte from the battery stored at 55 °C/100%SOC, resulting in obvious decline of its heat generation compared to that of the fresh anode, as presented in Table 7. That demonstrates the improved thermal stability of the anode stored at 55 °C/100%SOC, benefiting from the lower lithiation degree in the anode [58].

Fig. 10 presents the DSC profiles of sample cathode+anode and sample cathode. For batteries cycled at -5 °C/1C, a new exothermic peak between 100 °C and 200 °C was observed in the DSC profile of sample cathode+anode, with the heat generation increasing to 1661.5 J g⁻¹ (14.8% higher than that of the fresh electrodes). However, as shown in Fig. 10 (b) and Table 7, the DSC profile and the heat generation of the cathode cycled at -5 °C/1C remained nearly the same as those of the fresh cathode, thus demonstrating that the thermal stability of the cathode remained unchanged. Therefore, the new exothermic peak was induced by exothermic reaction related to the plated lithium on the anode surface, similar to Fig. 9. The DSC profiles and heat generation of the sample cathode+anode of the batteries degraded under the other three paths were similar with those of the fresh batteries, as presented in Fig. 10 and Table 7. Moreover, all the fresh and degraded cathodes exhibited similar DSC profiles and heat generation, indicating little changes in the thermal stability of the cathode during aging process. Therefore, the evolution of battery TR behavior during the whole life cycle mainly depended on the changes in the exothermic reactions between the anode and electrolyte.

3.4. TR behavior of fresh and degraded batteries

The temperature rate vs. temperature profiles of the fresh and degraded batteries during adiabatic TR tests are presented in Fig. 11.

The batteries cycled at -5 °C/1C exhibited a new exothermic peak in the temperature range of 50–120 °C, in which the temperature rate increased as SOH declined. According to the DSC tests results in Fig. 9, the new exothermic peak was induced by the reaction between plated lithium and electrolyte. Moreover, the batteries at 85% and 80% SOH showed serious deterioration of thermal stability compared to the fresh battery, with the temperature rate increasing obviously and the onset of TR shifting to much lower temperature.

In contrast, the temperature rate profiles of the batteries degraded under the other three aging paths exhibited only minor changes. The temperature rate profiles of batteries cycled at 25 °C/2C overlapped with that of the fresh battery until the SOH reached

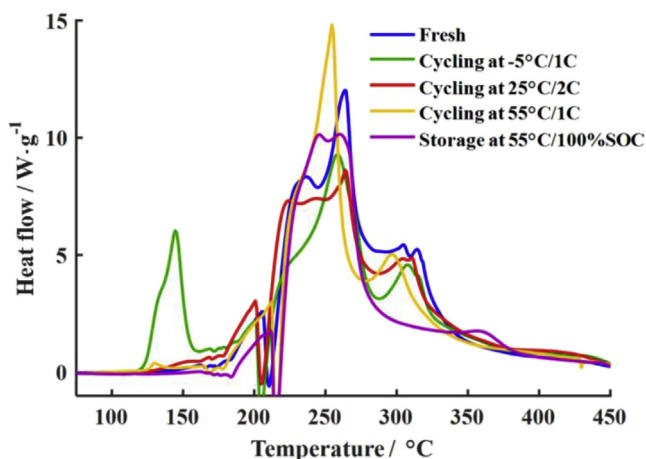


Fig. 9. DSC profiles of the samples anode+electrolyte of batteries at the BoL and EoL under different degradation paths.

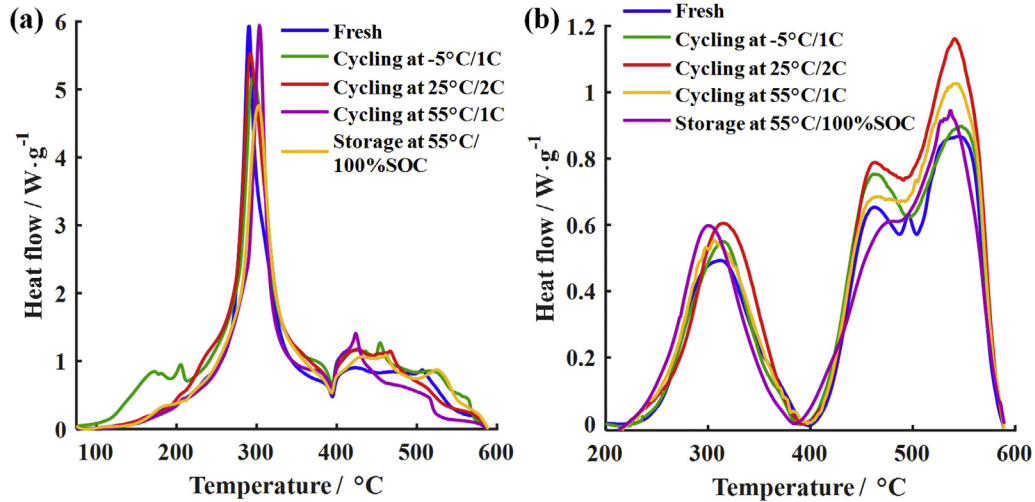


Fig. 10. DSC profiles of the sample cathode+anode and sample cathode of batteries at the BoL and EoL under different degradation paths. (a) sample cathode+anode; (b) sample cathode.

Table 7
Heat generation of the DSC test samples.

Degradation path	Heat generation/ $\text{J} \cdot \text{g}^{-1}$		
	anode+electrolyte	cathode+anode	cathode
Fresh	2599.9	1446.7	403.6
Cycling at $-5^\circ\text{C}/1\text{C}$	2457.0	1661.5	433.3
Cycling at $25^\circ\text{C}/2\text{C}$	2471.1	1550.2	471.8
Cycling at $55^\circ\text{C}/1\text{C}$	2377.9	1377.6	439.3
Storage at $55^\circ\text{C}/100\%\text{SOC}$	2084.9	1411.2	440.5

80%. The battery at 80%SOH showed higher temperature rate in the temperature range of 50–120 °C and a lowered onset temperature of TR, mainly due to the exothermic reaction between electrolyte and minor plated lithium on the anode, as indicated in DSC profile of sample anode+electrolyte in Fig. 9. The battery TR performance showed few changes during cycling at 55 °C/1C, as the temperature rate profiles of the degraded batteries overlapped with that of the fresh battery. The batteries stored at 55 °C/100%SOC showed improved TR performance, with the temperature rate between 70 and 170 °C decreasing gradually with the decline of SOH.

Four critical parameters including the critical temperature $\{T_1, T_2, T_3\}$ [6] and Δt_{TR} , are proposed to quantitatively evaluate the TR performance of lithium-ion batteries, as shown in Fig. 12. T_1 is the onset temperature of self-heating, which is defined as the temperature at which the self-heating rate of the battery exceeds $0.01^\circ\text{C} \cdot \text{min}^{-1}$; T_2 denotes the onset temperature of TR, which is defined as the temperature at which the battery temperature rate becomes higher than $1^\circ\text{C} \cdot \text{s}^{-1}$; T_3 is the maximum temperature during the TR process. Δt_{TR} is defined as the interval between T_{1f} and T_2 to evaluate the time required for the battery to go to thermal runaway under adiabatic condition. T_{1f} is the T_1 of the fresh battery. The calculation of Δt_{TR} is presented in the Appendix.

Fig. 13 presents the changes of the critical parameters $\{T_1, T_2, T_3, \Delta t_{\text{TR}}\}$ with SOH under the four different degradation paths. For the batteries cycled at $-5^\circ\text{C}/1\text{C}$, T_1 decreased from 72.39 °C to 52.40 °C when the SOH dropping from 100% to 77.5%. T_2 also dropped by 23 °C (from 213.3 °C to 190.2 °C) after cycling at $-5^\circ\text{C}/1\text{C}$, while T_3 remained constant at different SOH. Δt_{TR} became much shorter as the batteries degraded and decreased by 70% when SOH reached 80%. The changes of $\{T_1, T_2, T_3, \Delta t_{\text{TR}}\}$ indicate severe deterioration of battery TR performance after cycling at $-5^\circ\text{C}/1\text{C}$. According to

Sec.3.2, the batteries cycled at $-5^\circ\text{C}/1\text{C}$ suffered from severe lithium plating. The exothermic reaction between plated lithium and electrolyte begins at lower temperatures and generates a large amount of heat, leading to increment in temperature rate in Fig. 11 and thus obvious decreases in T_1 , T_2 , and Δt_{TR} . T_1 , T_2 , and Δt_{TR} of the batteries cycled at $25^\circ\text{C}/2\text{C}$ also decreased with SOH. For the battery degraded to EoL by cycling at $25^\circ\text{C}/2\text{C}$, T_1 and T_2 reduced to 60.0 °C and 190.2 °C, respectively. Δt_{TR} also dropped to only 58.9% of that in fresh batteries. That indicates that the batteries became more prone to TR. However, T_3 decreased significantly to 508.3 °C from 829.3 °C when the battery SOH reached 78.5%, presenting much smaller heat generation during TR process. According to Fig. 9, the decreases of T_1 , T_2 , and Δt_{TR} were attributed to the early onset of the exothermic reactions in sample anode+electrolyte due to lithium plating. The decline of T_3 after cycling at $25^\circ\text{C}/2\text{C}$ was benefited from electrolyte consumption, which reduced the heat generation of the reactions between the anode and electrolyte. The four critical parameters $\{T_1, T_2, T_3, \Delta t_{\text{TR}}\}$ of the batteries cycled at $55^\circ\text{C}/1\text{C}$ remained almost unchanged, which is consistent with the DSC tests results in Sec.3.3. Therefore, the side reactions inside the battery during cycling at $55^\circ\text{C}/1\text{C}$ have little impact on the TR performance. The batteries stored at $55^\circ\text{C}/100\%\text{SOC}$ showed improved TR performance, with T_1 rising to 96.3 °C and Δt_{TR} reaching 2.85 times its initial value. According to Sec.3.2, the anodes had lower lithiation degree after high-temperature storage, resulting in the delayed onset temperature and reduced heat generation in the early stage of the battery TR process.

3.5. Discussion

The effects of the side reactions on the battery degradation mode and TR performance are summarized in Fig. 14. During the aging process of the 24Ah lithium-ion battery, side reactions at the cathode included secondary particle cracking, CEI film formation and transition metal dissolution, while the anode suffered from SEI film thickening and lithium plating. Electrolyte consumption also occurred during cycling at $25^\circ\text{C}/2\text{C}$, leading to a drastic increase in the impedance. The side reactions at the cathode lead to LAM at cathode, and CEI film formation also induces impedance increment by hindering the charge transfer process on the cathode surface [59]. Moreover, the dissolved transition metal from the cathode can deposit on the anode and accelerate SEI film growth, resulting in LLI

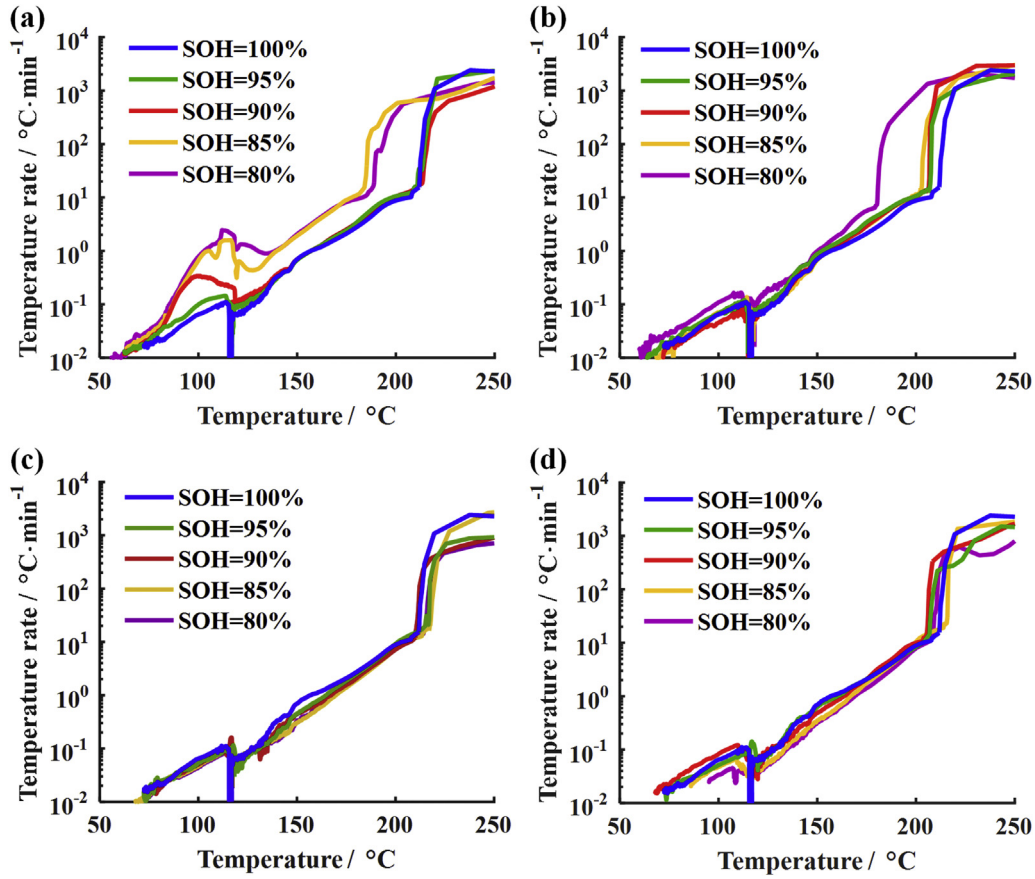


Fig. 11. Evolution of battery TR behavior under different degradation paths. (a) cycling at $-5\text{ }^{\circ}\text{C}/1\text{C}$; (b) cycling at $25\text{ }^{\circ}\text{C}/2\text{C}$; (c) cycling at $55\text{ }^{\circ}\text{C}/1\text{C}$; (d) storage at $55\text{ }^{\circ}\text{C}/100\%\text{SOC}$.

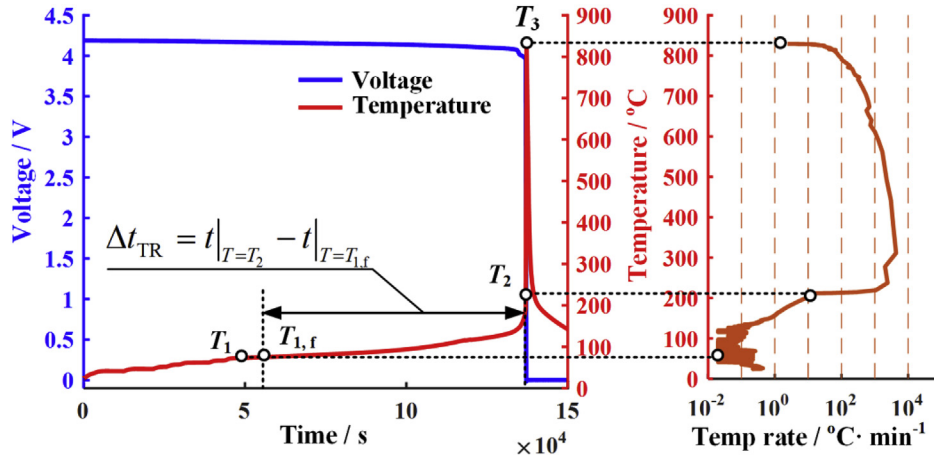


Fig. 12. The critical parameters $\{T_1, T_2, T_3, \Delta t_{\text{TR}}\}$ of lithium-ion during TR process.

[54]. For the anode, SEI film thickening and lithium plating both consume lithium inventory and result in LLI [45,46]. The products from SEI film thickening and the reaction between plated lithium and electrolyte will further reduce anode porosity, leading to LAM at anode and impedance increment [60].

During aging process, the evolution of the battery TR performance mainly depends on the changes in the thermal stability of the anode+electrolyte thermodynamic system, whereas the side reactions at the cathode have little impact. Lithium plating on the anode leads to severe deterioration of the battery TR performance,

with drastic increase in the temperature rate and obvious decrease in T_1 , T_2 , and Δt_{TR} . SEI film thickening consumes lithium inventory, thus reducing the lithiation degree of the anode. The anode with a lower lithiation degree is more thermally stable [58] and leads to improved battery TR performance with increased T_1 and a lower temperature rate. Furthermore, electrolyte consumption reduces the heat generation from the reactions between the anode and electrolyte, resulting in a significant decrease of T_3 .

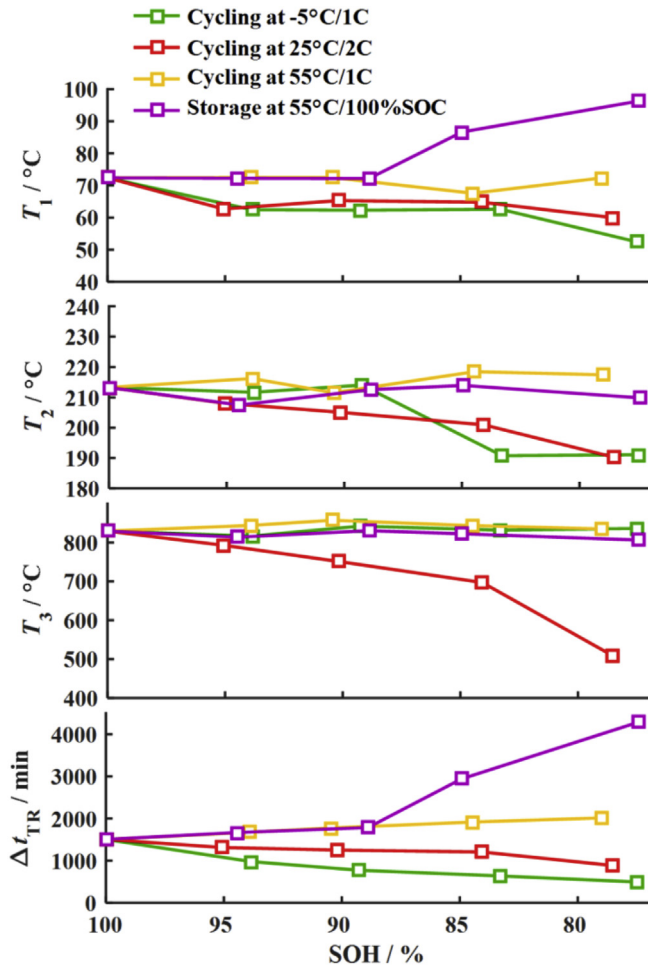


Fig. 13. Changes of the critical parameters ($T_1, T_2, T_3, \Delta t_{TR}$) with SOH under different degradation paths.

4. Conclusion

The aging effects on the TR behavior of 24Ah commercial lithium-ion batteries are investigated in this paper. The batteries

were degraded under four different aging paths. Post-mortem analysis on the electrochemical properties, morphology and composition of the fresh and degraded electrodes was conducted to reveal the aging mechanism. The changes in electrode thermal stability were evaluated through DSC tests. Furthermore, 34 TR tests were performed on the batteries at various SOH under different degradation paths. Finally, the correlations between the degradation mechanism and the changes in battery TR performance are summarized.

The battery degradation behavior and mechanism under four kinds of aging tests (including cycling at $-5^\circ\text{C}/1\text{C}$, $25^\circ\text{C}/2\text{C}$, $55^\circ\text{C}/1\text{C}$, and storage at $55^\circ\text{C}/100\%\text{SOC}$) were investigated based on the electrochemical characterization and SEM, XPS, ICP-OES and NMR analysis on the degraded electrodes. The batteries cycled at $-5^\circ\text{C}/1\text{C}$ showed rapid degradation and suffered from severe LLI, due to lithium plating on the anode surface. The batteries cycled at $25^\circ\text{C}/2\text{C}$ experienced severe electrolyte consumption, as well as several side reactions at both cathode and anode. As a result, rapid increases of ohmic and charge transfer resistances took place in batteries cycled at $25^\circ\text{C}/2\text{C}$, along with LAM at both cathode and anode. The batteries cycled $55^\circ\text{C}/1\text{C}$ exhibited complex degradation mode, with LAM at both electrodes, LLI, and impedance increment. The cathode suffered from secondary particle cracking and CEI film formation, while the anode exhibited SEI film thickening. For the batteries stored at $55^\circ\text{C}/100\%\text{SOC}$, SEI film thickening was the dominant side reaction, resulting in obvious LLI.

The changes in the battery TR performance were characterized through DSC and TR tests. The thermal stability of the degraded cathodes was found to remain nearly the same as that of the fresh cathode. Thus, the evolution of battery TR features mainly depends on the changes in the thermal stability of the anode+electrolyte thermodynamic system. The TR features and the temperature rate profiles of the batteries cycled at $55^\circ\text{C}/1\text{C}$ remained the same as those of a fresh battery, whereas the degraded batteries under the other three degradation paths all showed changes in TR behavior. The batteries cycled at $-5^\circ\text{C}/1\text{C}$ exhibited serious deterioration of TR performance, with a new exothermic peak related to plated lithium in the temperature rate profiles and an obvious decrease of T_1 , T_2 , and Δt_{TR} , while T_3 remained unchanged. Significant decrease of T_3 occurred in the batteries cycled at $25^\circ\text{C}/2\text{C}$, due to the electrolyte consumption. The batteries cycled at $25^\circ\text{C}/2\text{C}$ also showed decrease of T_1 , T_2 and Δt_{TR} when SOH dropped to 78.5%, due to lithium plating on the anode. The batteries stored at $55^\circ\text{C}/100\%\text{SOC}$

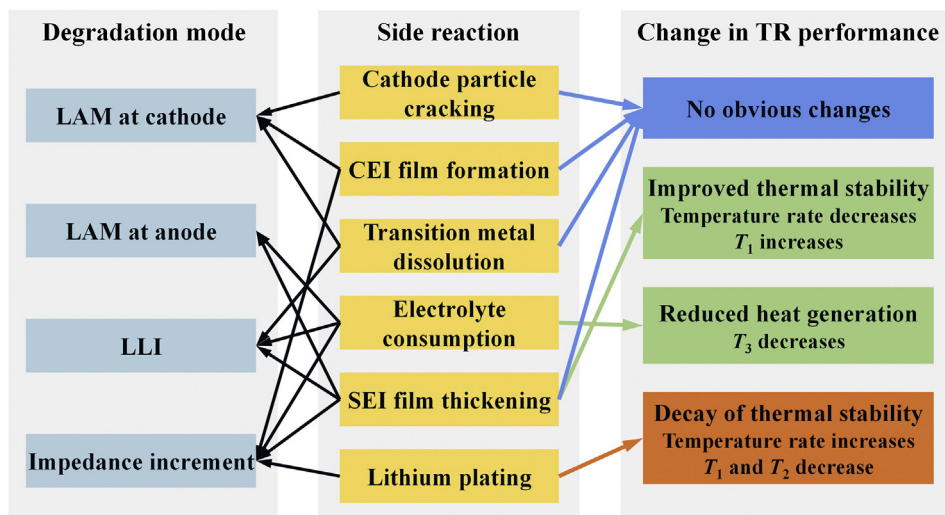


Fig. 14. Summary of the effects of side reactions on battery degradation mode and changes in TR performance.

showed improved TR performance, with a significant increase in T_1 and Δt_{TR} , as well as a lower temperature rate in the early stage of TR. That was attributed to the decrease of lithiation degree of the anode after high-temperature storage.

Finally, the correlations between the aging mechanism and the changes in the TR behavior are summarized. Side reactions at the cathode (including particle cracking, CEI film formation and transition metal dissolution, etc.) have few effects on battery TR performance. SEI film thickening reduces the lithiation degree of the fully-charged anode, resulting in improved battery TR performance, whereas electrolyte consumption lead to a significant decrease of heat generation during the battery TR process. Lithium plating turns out to be the key reason for the deterioration of battery TR performance.

Future work will focus on quantitative analysis of the effects of lithium plating on battery TR performance, and TR model to predict the changes in battery TR behavior during whole life cycle.

Declaration of competing interest

The authors declare that they have no known competing financial interests or personal relationships that could have appeared to influence the work reported in this paper.

Acknowledgement

This work is supported by the National Key R&D Program of China (2018YFB0104000) and the National Natural Science Foundation of China (No. U1564205, 51706117, and 51807108), and funded by the Beijing Natural Science Foundation under the Grant No. 3184052.

Appendix. Calculation of Δt_{TR} during the TR process

Due to the low temperature rate and long duration during the initial stage of TR process, the interval between T_1 and T_2 is greatly affected by T_1 . Therefore, this research defines the critical parameter Δt_{TR} as the interval for the battery temperature increase from $T_{1,f}$ to T_2 by self-heating, such that the time required for the battery to go to TR under adiabatic condition could be evaluated on the same basis. $T_{1,f} = 72.39^\circ\text{C}$ is the T_1 of the fresh battery.

The calculation of Δt_{TR} can be divided into two cases according to the value of T_1 and $T_{1,f}$.

Case 1 ($T_1 \leq T_{1,f}$): the calculation of Δt_{TR} is simple in this case, as in Eq.(A-1). $t|_{T=T_{1,f}}$ and $t|_{T=T_2}$ is the time when the battery temperature reaches $T_{1,f}$ and T_2 during the TR process, respectively.

Case 2 ($T_1 > T_{1,f}$): Δt_{TR} can be divided into two parts, namely Δt_{est} and $t|_{T=T_2} - t|_{T=T_1}$, as shown in Eq.(A-2). Δt_{est} is the estimated interval for the battery to heat itself from $T_{1,f}$ to T_1 under adiabatic conditions, and $t|_{T=T_2} - t|_{T=T_1}$ is the interval between T_1 and T_2 . The calculation of Δt_{est} is presented in Eq.(A-3) and Fig. A1. T_{si} and $\frac{dT}{dt}|_{T=T_{si}}$ ($i = 0, 1, 2, 3, \dots, n$) represent the battery temperature and temperature rate at the end of each heat-wait-see cycle, respectively. $T_{s0} \leq T_{1,f} \leq T_{s1}$, and $T_{sn} = T_1$. EV-ARC can maintain the adiabatic condition during the seek period. Therefore, $\frac{dT}{dt}|_{T=T_{si}}$ can be regarded as the self-heating rate of the tested battery at T_{si} . Assuming that the increase of battery temperature rate follows a linear trend at the initial stage of self-heating, the interval for the battery temperature to increase from T_{si} to T_{si+1} can thus be estimated by dividing the temperature difference ($T_{si+1} - T_{si}$) through the average temperature rate $\frac{1}{2}(\frac{dT}{dt}|_{T=T_{si}} + \frac{dT}{dt}|_{T=T_{si+1}})$. Then, Δt_{est} can be calculated using Eq.(A-3).

$$\Delta t_{TR} = t|_{T=T_2} - t|_{T=T_{1,f}} \quad T_1 \leq T_{1,f} \quad (\text{A-1})$$

$$\Delta t_{TR} = \Delta t_{est} + t|_{T=T_2} - t|_{T=T_1} \quad T_1 > T_{1,f} \quad (\text{A-2})$$

$$\Delta t_{est} = \frac{2(T_{s1} - T_{1,f})}{\frac{dT}{dt}|_{T=T_{s0}} + \frac{dT}{dt}|_{T=T_{s1}}} + \frac{2(T_{s2} - T_{s1})}{\frac{dT}{dt}|_{T=T_{s1}} + \frac{dT}{dt}|_{T=T_{s2}}} + \frac{2(T_{s3} - T_{s2})}{\frac{dT}{dt}|_{T=T_{s2}} + \frac{dT}{dt}|_{T=T_{s3}}} + \dots + \frac{2(T_1 - T_{sn-1})}{\frac{dT}{dt}|_{T=T_{sn-1}} + \frac{dT}{dt}|_{T=T_{sn}}} \quad (\text{A-3})$$

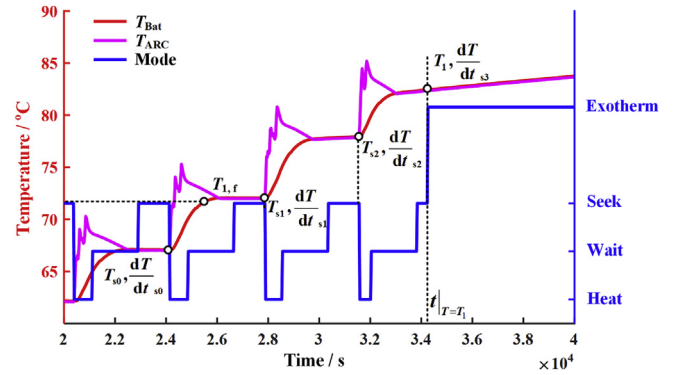


Fig. A1. Illustration of the calculation of Δt_{est} .

References

- [1] Feng X, Ouyang M, Liu X, Lu L, Xia Y, He X. Thermal runaway mechanism of lithium ion battery for electric vehicles: a review. *Energy Storage Mater* 2018;10:246–67. <https://doi.org/10.1016/j.ensm.2017.05.013>.
- [2] Lithium-ion Power Battery Safety Research Report. Battery Safety Laboratory at Tsinghua University; 2019. in chinese, http://www.sohu.com/a/335424046_733088.
- [3] Liu L, Xu J, Wang S, Wu F, Li H, Chen L. Practical evaluation of energy densities for sulfide solid-state batteries. *eTransportation* 2019;1:100010. <https://doi.org/10.1016/j.etrans.2019.100010>.
- [4] Lu L, Han X, Li J, Hua J, Ouyang M. A review on the key issues for lithium-ion battery management in electric vehicles. *J Power Sources* 2013;226:272–88. <https://doi.org/10.1016/j.jpowsour.2012.10.060>.
- [5] Feng X, Zheng S, He X, Wang L, Wang Y, Ren D, et al. Time sequence map for interpreting the thermal runaway mechanism of lithium-ion batteries with $\text{LiNi}_{0.8}\text{Co}_{0.1}\text{Mn}_{0.1}\text{O}_2$ cathode. *Front Energy Res* 2018;6:1–16. <https://doi.org/10.3389/fenrg.2018.00126>.
- [6] Feng X, Zheng S, Ren D, He X, Wang L, Cui H, et al. Investigating the thermal runaway mechanisms of lithium-ion batteries based on thermal analysis database. *Appl Energy* 2019;246:53–64. <https://doi.org/10.1016/j.apenergy.2019.04.009>.
- [7] Zheng S, Wang L, Feng X, He X. Probing the heat sources during thermal runaway process by thermal analysis of different battery chemistries. *J Power Sources* 2018;378:527–36. <https://doi.org/10.1016/j.jpowsour.2017.12.050>.
- [8] Ren D, Liu X, Feng X, Lu L, Ouyang M, Li J, et al. Model-based thermal runaway prediction of lithium-ion batteries from kinetics analysis of cell components. *Appl Energy* 2018;228:633–44. <https://doi.org/10.1016/j.apenergy.2018.06.126>.
- [9] Feng X, Fang M, He X, Ouyang M, Lu L, Wang H, et al. Thermal runaway features of large format prismatic lithium ion battery using extended volume accelerating rate calorimetry. *J Power Sources* 2014;255:294–301. <https://doi.org/10.1016/j.jpowsour.2014.01.005>.
- [10] Roth EP, Doughty DH. Thermal abuse performance of high-power 18650 Li-ion cells. *J Power Sources* 2004;128:308–18. <https://doi.org/10.1016/j.jpowsour.2003.09.068>.
- [11] Richard MN, Dahn JR. Accelerating rate calorimetry study on the thermal stability of lithium intercalated graphite in electrolyte. I. Experimental. *J Electrochem Soc* 1999;146:2068–77. <https://doi.org/10.1149/1.1391894>.
- [12] Richard MN, Dahn JR. Accelerating rate calorimetry study on the thermal stability of lithium intercalated graphite in electrolyte. II. Modeling the results and predicting differential scanning calorimeter curves. *J Electrochem Soc* 1999;146:2078–84. <https://doi.org/10.1149/1.1391894>.
- [13] Feng X, Sun J, Ouyang M, He X, Lu L, Han X, et al. Characterization of large format lithium ion battery exposed to extremely high temperature. *J Power Sources* 2014;272:457–67. <https://doi.org/10.1016/j.jpowsour.2014.08.094>.
- [14] Chen Z, Qin Y, Ren Y, Lu W, Orendorff C, Roth EP, et al. Multi-scale study of the thermal stability of lithiated graphite. *Energy Environ Sci* 2011;4:4023–30. <https://doi.org/10.1039/c1ee01786a>.

- [15] Yang H, Bang H, Amine K, Prakash J. Investigations of the exothermic reactions of natural graphite anode for Li-ion batteries during thermal runaway. *J Electrochem Soc* 2005;152:A73–9. <https://doi.org/10.1149/1.1836126>.
- [16] Forestier C, Grugeon S, Davoine C, Lecocq A, Marlair G, Armand M, et al. Graphite electrode thermal behavior and solid electrolyte interphase investigations: role of state-of-the-art binders, carbonate additives and lithium bis(fluorosulfonyl)imide salt. *J Power Sources* 2016;330:186–94. <https://doi.org/10.1016/j.jpowsour.2016.09.005>.
- [17] Yamaki JI, Takatsui H, Kawamura T, Egashira M. Thermal stability of graphite anode with electrolyte in lithium-ion cells. *Solid State Ion* 2002;148:241–5. [https://doi.org/10.1016/S0167-2738\(02\)00060-7](https://doi.org/10.1016/S0167-2738(02)00060-7).
- [18] Bak S, Hu E, Zhou Y, Yu X, Senanayake SD, Cho S, et al. Structural changes and thermal stability of charged $\text{LiNi}_{0.8}\text{Mn}_{0.2}\text{Co}_2\text{O}_2$ cathode materials studied by combined in situ time-resolved XRD and mass spectroscopy. *ACS Appl Mater Interfaces* 2014;6:22594–601. <https://doi.org/10.1021/am506712c>.
- [19] Nam K-W, Bak S-M, Hu E, Yu X, Zhou Y, Wang X, et al. Combining in situ synchrotron X-ray diffraction and absorption techniques with transmission electron microscopy to study the origin of thermal instability in overcharged cathode materials for lithium-ion batteries. *Adv Funct Mater* 2013;23:1047–63. <https://doi.org/10.1002/adfm.201200693>.
- [20] Yamaki J-i, Shinjo Y, Doi T, Okada S. The rate equation for oxygen evolution by decomposition of Li_2CoO_2 at elevated temperatures. *J Electrochem Soc* 2014;161:A1648–54. <https://doi.org/10.1149/2.0621410jes>.
- [21] Ren D, Feng X, Lu L, He X, Ouyang M. Overcharge behaviors and failure mechanism of lithium-ion batteries under different test conditions. *Appl Energy* 2019;250:323–32. <https://doi.org/10.1016/j.apenergy.2019.05.015>.
- [22] Belharouak I, Vissers D, Amine K. Thermal stability of the $\text{Li}(\text{Ni}_{0.8}\text{Co}_{0.15}\text{Al}_{0.05})\text{O}_2$ cathode in the presence of cell components. *J Electrochem Soc* 2006;153:A2030–5. <https://doi.org/10.1149/1.2336994>.
- [23] Huang Q, Ma L, Liu A, Ma X, Li J, Wang J, et al. The reactivity of charged positive $\text{Li1-n}[\text{NiMnCo}]_2\text{O}_2$ electrodes with electrolyte at elevated temperatures using accelerating rate calorimetry. *J Power Sources* 2018;390:78–86. <https://doi.org/10.1016/j.jpowsour.2018.04.036>.
- [24] Wang Y, Jiang J, Dahn JR. The reactivity of delithiated $\text{Li}(\text{Ni}_{1/3}\text{Co}_{1/3}\text{Mn}_{1/3})\text{O}_2$, $\text{Li}(\text{Ni}_{0.8}\text{Co}_{0.15}\text{Al}_{0.05})\text{O}_2$ or LiCoO_2 with non-aqueous electrolyte. *Electrochem Commun* 2007;9:2534–40. <https://doi.org/10.1016/j.elecom.2007.07.033>.
- [25] Liu X, Ren D, Hsu H, Feng X, Xu GL, Zhuang M, et al. Thermal runaway of lithium-ion batteries without internal short circuit. *Joule* 2018;1:1–18. <https://doi.org/10.1016/j.joule.2018.06.015>.
- [26] Inoue T, Mukai K. Are all-solid-state lithium-ion batteries really Safe ? – verification by differential scanning calorimetry with an all-inclusive microcell. *ACS Appl Mater Interfaces* 2017;9:1507–15. <https://doi.org/10.1021/acsami.6b13224>.
- [27] Inoue T, Mukai K. Roles of positive or negative electrodes in the thermal runaway of lithium-ion batteries: accelerating rate calorimetry analyses with an all-inclusive microcell. *Electrochem Commun* 2017;77:28–31. <https://doi.org/10.1016/j.elecom.2017.02.008>.
- [28] Roth EP, Crafts C, Doughty D, McBrean J. Advanced Technology development Program for lithium-ion batteries: thermal abuse performance of 18650 Li-ion cells. *Sandia Natl Lab* 2004;1–139. <https://doi.org/10.2172/918751>.
- [29] Börner M, Friesen A, Grütze M, Stenzel YP, Brunklaus G, Haetge J, et al. Correlation of aging and thermal stability of commercial 18650-type lithium ion batteries. *J Power Sources* 2017;342:382–92. <https://doi.org/10.1016/j.jpowsour.2016.12.041>.
- [30] Zhang Y, Xiong R, He H, Qu X, Pecht M. Aging characteristics-based health diagnosis and remaining useful life prognostics for lithium-ion batteries. *eTransportation* 2019;1:100004. <https://doi.org/10.1016/j.etrans.2019.100004>.
- [31] Fleischhammer M, Waldmann T, Bisle G, Hogg B-I, Wohlfahrt-Mehrens M. Interaction of cyclic ageing at high-rate and low temperatures and safety in lithium-ion batteries. *J Power Sources* 2015;274:432–9. <https://doi.org/10.1016/j.jpowsour.2014.08.135>.
- [32] Waldmann T, Quinn JB, Richter K, Kasper M, Tost A, Klein A, et al. Electrochemical, post-mortem, and ARC analysis of Li-ion cell safety in second-life applications. *J Electrochem Soc* 2017;164:A3154–62. <https://doi.org/10.1149/2.0961713jes>.
- [33] Feng X, Ren D, Zhang S, He X, Wang L, Ouyang M. Influence of aging paths on the thermal runaway features of lithium-ion batteries in accelerating rate calorimetry tests. *Int J Electrochem Sci* 2019;14:44–58. <https://doi.org/10.20964/2019.01.14>.
- [34] Tobishima S, Yamaki J, Hirai T. Safety and capacity retention of lithium ion cells after long periods of storage. *J Appl Electrochem* 2000;30:405–10. <https://doi.org/10.1023/A:1003992027121>.
- [35] Wu Y-F, Brun-Buisson D, Genies S, Mattera F, Merten J. Thermal behavior of lithium-ion cells by adiabatic calorimetry: one of the selection criteria for all applications of storage. *ECS Trans* 2009;16:93–103. <https://doi.org/10.1149/1.3115311>.
- [36] Zhang J, Su L, Li Z, Sun Y, Wu N. The evolution of lithium-ion cell thermal safety with aging examined in a battery testing calorimeter. *Batteries* 2016;2:12. <https://doi.org/10.3390/batteries2020012>.
- [37] Hildebrand S, Rheinfeld A, Friesen A, Haetge J, Schappacher FM, Jossen A, et al. Thermal analysis of $\text{LiNi}_{0.4}\text{Co}_{0.2}\text{Mn}_{0.4}\text{O}_2$ /mesocarbon microbeads cells and electrodes: state-of-charge and state-of-health influences on reaction kinetics. *J Electrochem Soc* 2018;165:A104–17. <https://doi.org/10.1149/2.0361802jes>.
- [38] Friesen A, Hildebrand S, Horsthemke F, Börner M, Klöpsch R, Niehoff P, et al. Al_2O_3 coating on anode surface in lithium ion batteries: impact on low temperature cycling and safety behavior. *J Power Sources* 2017;363:70–7. <https://doi.org/10.1016/j.jpowsour.2017.07.062>.
- [39] Friesen A, Horsthemke F, Mönnighoff X, Brunklaus G, Krafft R, Börner M, et al. Impact of cycling at low temperatures on the safety behavior of 18650-type lithium ion cells: combined study of mechanical and thermal abuse testing accompanied by post-mortem analysis. *J Power Sources* 2016;334:1–11. <https://doi.org/10.1016/j.jpowsour.2016.09.120>.
- [40] Waldmann T, Wohlfahrt-Mehrens M. Effects of rest time after Li plating on safety behavior—ARC tests with commercial high-energy 18650 Li-ion cells. *Electrochim. Acta* 2017;230:454–60. <https://doi.org/10.1016/j.electacta.2017.02.036>.
- [41] Tomaszewska A, Chu Z, Feng X, O’Kane S, Liu X, Chen J, et al. Lithium-ion battery fast charging: a review. *ETransportation* 2019;1:100011. <https://doi.org/10.1016/j.etrans.2019.100011>.
- [42] Ren D, Feng X, Lu L, Ouyang M, Zheng S, Li J, et al. An electrochemical-thermal coupled overcharge-to-thermal-runaway model for lithium ion battery. *J Power Sources* 2017;364:328–40. <https://doi.org/10.1016/j.jpowsour.2017.08.035>.
- [43] Ren D, Smith K, Guo D, Han X, Feng X, Lu L, et al. Investigation of lithium plating-stripping process in Li-ion batteries at low temperature using an electrochemical model. *J Electrochem Soc* 2018;165:A2167–78. <https://doi.org/10.1149/2.0661810jes>.
- [44] Ouyang M, Ren D, Lu L, Li J, Feng X, Han X, et al. Overcharge-induced capacity fading analysis for large format lithium-ion batteries with $\text{Li}_y\text{Ni}_{1/3}\text{Co}_{1/3}\text{Mn}_{1/3}\text{O}_2 + \text{Li}_y\text{Mn}_2\text{O}_4$ composite cathode. *J Power Sources* 2015;279:626–35. <https://doi.org/10.1016/j.jpowsour.2015.01.051>.
- [45] Han X, Ouyang M, Lu L, Li J, Zheng Y, Li Z. A comparative study of commercial lithium ion battery cycle life in electrical vehicle: aging mechanism identification. *J Power Sources* 2014;251:38–54. <https://doi.org/10.1016/j.jpowsour.2013.11.029>.
- [46] Han X, Lu L, Zheng Y, Feng X, Li Z, Li J, et al. A review on the key issues of the lithium ion battery degradation among the whole life cycle. *ETransportation* 2019;1:100005. <https://doi.org/10.1016/j.etrans.2019.100005>.
- [47] Ouyang M, Feng X, Han X, Lu L, Li Z, He X. A dynamic capacity degradation model and its applications considering varying load for a large format Li-ion battery. *Appl Energy* 2016;165:48–59. <https://doi.org/10.1016/j.apenergy.2015.12.063>.
- [48] Yan P, Zheng J, Gu M, Xiao J, Zhang JG, Wang CM. Intragranular cracking as a critical barrier for high-voltage usage of layer-structured cathode for lithium-ion batteries. *Nat Commun* 2017;8:1–9. <https://doi.org/10.1038/ncomms14101>.
- [49] Liu T, Garsuch A, Chesneau F, Lucht BL. Surface phenomena of high energy $\text{Li}(\text{Ni}_{1/3}\text{Co}_{1/3}\text{Mn}_{1/3})\text{O}_2$ /graphite cells at high temperature and high cutoff voltages. *J Power Sources* 2014;269:920–6. <https://doi.org/10.1016/j.jpowsour.2014.07.051>.
- [50] Genieser R, Loveridge M, Bhagat R. Practical high temperature (80 °C) storage study of industrially manufactured Li-ion batteries with varying electrolytes. *J Power Sources* 2018;386:85–95. <https://doi.org/10.1016/j.jpowsour.2018.03.050>.
- [51] Verma P, Maire P, Novák P. A review of the features and analyses of the solid electrolyte interphase in Li-ion batteries. *Electrochim Acta* 2010;55:6332–41. <https://doi.org/10.1016/j.electacta.2010.05.072>.
- [52] Bodenes L, Dedryvère R, Martinez H, Fischer F, Tessier C, Pèrès JP. Lithium-ion batteries working at 85 °C: aging phenomena and electrode/electrolyte interfaces studied by XPS. *J Electrochem Soc* 2012;159:1739–46. <https://doi.org/10.1149/2.061210jes>.
- [53] Ouyang M, Chu Z, Lu L, Li J, Han X, Feng X, et al. Low temperature aging mechanism identification and lithium deposition in a large format lithium iron phosphate battery for different charge profiles. *J Power Sources* 2015;286:309–20. <https://doi.org/10.1016/j.jpowsour.2015.03.178>.
- [54] Zheng H, Sun Q, Liu G, Song X, Battaglia VS. Correlation between dissolution behavior and electrochemical cycling performance for $\text{LiNi}_{1/3}\text{Co}_{1/3}\text{Mn}_{1/3}\text{O}_2$ -based cells. *J Power Sources* 2012;207:134–40. <https://doi.org/10.1016/j.jpowsour.2012.01.122>.
- [55] Zhan C, Wu T, Lu J, Amine K. Dissolution, Migration, and deposition of transition metal ions in Li-ion batteries exemplified by Mn-based cathodes- a critical review. *Energy Environ Sci* 2017. <https://doi.org/10.1039/C7EE03122J>.
- [56] Chevallier F, Poli F, Montigny B, Letellier M. In situ ^7Li nuclear magnetic resonance observation of the electrochemical intercalation of lithium in graphite: second cycle analysis. *Carbon N. Y.* 2013;61:140–53. <https://doi.org/10.1016/j.carbon.2013.04.078>.
- [57] Gotoh K, Izuka M, Arai J, Okada Y, Sugiyama T, Takeda K, et al. In situ ^7Li nuclear magnetic resonance study of the relaxation effect in practical lithium ion batteries. *Carbon N. Y.* 2014;79:380–7. <https://doi.org/10.1016/j.carbon.2014.07.080>.
- [58] Mukai K, Inoue T, Hasegawa M. Rationalizing thermal reactions of C_6Li_x negative electrode with nonaqueous electrolyte. *J Power Sources* 2017;366:185–92. <https://doi.org/10.1016/j.jpowsour.2017.09.027>.
- [59] Qian Y, Niehoff P, Börner M, Grütze M, Mönnighoff X, Behrends P, et al. Influence of electrolyte additives on the cathode electrolyte interphase (CEI) formation on $\text{LiNi}_{1/3}\text{Mn}_{1/3}\text{Co}_{1/3}\text{O}_2$ in half cells with Li metal counter electrode. *J Power Sources* 2016;329:31–40. <https://doi.org/10.1016/j.jpowsour.2016.08.023>.
- [60] Arora P, White RE, Doyle M. Capacity fade mechanisms and side reactions in lithium-ion batteries. *J Electrochem Soc* 1998;145:3647–67. <https://doi.org/10.1149/1.1838857>.